

# Time-resolved high-harmonic spectroscopy of valence electron dynamics

Peter M. Kraus, Hans Jakob Wörner\*

Laboratorium für Physikalische Chemie, ETH Zürich, Wolfgang-Pauli-Strasse 10, 8093 Zürich, Switzerland

## ARTICLE INFO

### Article history:

Available online 16 February 2012

Dedicated to Prof. W. van Gunsteren on the occasion of his 65th birthday.

### Keywords:

High-harmonic generation  
High-harmonic spectroscopy  
Attosecond science  
Time-resolved spectroscopy  
Photochemical dynamics  
Photodissociation  
Conical intersections  
Non-adiabatic dynamics

## ABSTRACT

Time-resolved high-harmonic spectroscopy (TRHHS) is an emerging technique for probing valence electron dynamics in molecules undergoing photochemical reactions. A general description of the technique including experimental and theoretical aspects is given. The relation of TRHHS to other time-resolved techniques is discussed, with particular emphasis on the specificities of TRHHS. Coherence endows TRHHS with two of its original properties: the interference of excited and unexcited molecules makes it highly sensitive to small excitation fractions and to the phase of photorecombination matrix elements. The technique is also sensitive to the variation of the vertical ionization potential, providing additional insights into the photochemical dynamics. The principles of the technique are discussed in relation to recent results on the photochemistry of Br<sub>2</sub> and NO<sub>2</sub>, revealing its sensitivity to different aspects of the dynamics, most notably electronic dynamics occurring in non-adiabatic dynamics.

© 2012 Elsevier B.V. All rights reserved.

## 1. Introduction

The valence electronic structure of molecules defines both their shape and their reactivity. A chemical reaction is often rationalized in terms of trajectories of nuclear wave packets over electronic potential energy surfaces. Hence, time-resolved spectroscopy has to address two main aspects of the dynamics. Most intuitively, the motion of the atoms relative to each other needs to be understood. This motion will in most cases be determined by the local shape of the potential energy surface which results from the electronic structure of the molecule. Hence, experimental methods are required that probe the valence shell of the molecule and the evolution of its structure along the chemical reaction pathway.

Many powerful approaches have been developed over the past decades for studying the internal motion of atoms in molecules [1,2]. The most recent developments include X-ray scattering [3,4] and electron scattering [5,6] which have advanced the field to studying highly complex systems, including very large molecules and solids. Far fewer methods exist that directly probe the valence shell of molecules on a femtosecond time scale. Time-resolved photoelectron spectroscopy (TRPES) [7] and time-resolved X-ray absorption spectroscopy (TRXAS) [8] have recently provided important insights into the valence structure of molecules. In the gas phase, TRPES has been extended to measure photoelectron angular distributions (PADs) [9–11] which provide additional de-

tails about the electronic structure, particularly when the measurement can be done in the molecular frame [12,13].

In this article we discuss a complementary emerging technique for probing the dynamics of the molecular valence shell which uses high-harmonic generation (HHG) in a strong laser field as a probe. Over the last 10 years, HHG has been developed into a useful approach for measuring the structure and dynamics of molecules. The combination of HHG with impulsive stimulated Raman scattering has yielded a wide range of applications, exploiting rotational or vibrational wave packets prepared in the electronic ground state. Rotational wave packets offer a way of fixing the molecular axes in space and performing HHG measurements in the molecular frame. Such measurements have established the sensitivity of HHG to the electronic structure of the target. Vibrational wave packets have been shown to modulate the yield of HHG which has been attributed to the coordinate dependence of the electronic structure of the studied molecules [14–16]. In 2010, HHG has been first applied to study dynamics in electronically excited states using either collinear pump and probe pulses [17] or a transient grating geometry [18], studying the photodissociation of Br<sub>2</sub>. Most recently, the method has been applied to non-adiabatic photodissociation dynamics of NO<sub>2</sub>, revealing the variation of the electronic character of the molecule caused by traversing a conical intersection [19].

Here, we describe the general principles of TRHHS from both experimental and theoretical perspectives. We formulate a general framework for the interpretation and simulation of the observables and compare recent experimental results with simple model

\* Corresponding author.

E-mail address: [woerner@phys.chem.ethz.ch](mailto:woerner@phys.chem.ethz.ch) (H.J. Wörner).

calculations. We study the sensitivity of TRHHS to the coordinate-dependence of strong-field ionization rates, vertical ionization potentials and photorecombination matrix elements and discuss the role of wave packet delocalization in low- and high-dimensional coordinate spaces. This study enables us to draw important conclusions about the working principles of TRHHS and its possible future applications.

## 2. Theoretical formulation

### 2.1. High-harmonic spectroscopy

The high-harmonic generation signal emitted from a molecule can be described as resulting from strong-field ionization followed by propagation of the electron in the laser field and photorecombination. Each step contributes an amplitude and a phase to the induced dipole moment which can be represented in terms of its complex spectral representation as

$$\tilde{d}(\Omega, \phi, \theta, \chi) \propto \sum_f a_{\text{ion},f}(\phi, \theta, \chi) a_{\text{prop},f}(\Omega, \phi, \theta, \chi) a_{\text{rec},f}(\Omega, \phi, \theta, \chi), \quad (1)$$

where  $\Omega$  is the emitted photon frequency (equal to multiples of the fundamental),  $\phi, \theta, \chi$  are the Euler angles representing the orientation of the molecule-fixed axis system in space and the sum runs over the states of the cation that are accessible in the strong-field ionization step. Here and throughout this article we use atomic units. Here and throughout this article we use atomic units. We will not explicitly write the dependence on the Euler angles in the following to keep the notation simple, but it is of course taken into account in the calculations described below.

The term  $a_{\text{rec},f}$  is best approximated as complex photorecombination matrix element in the molecular frame, which is obtained from quantum scattering calculations in the effective potential corresponding to the cation state  $f$  [20–22]. The terms  $a_{\text{ion},f}$  and  $a_{\text{prop},f}$  can be either evaluated separately or the product  $a_{\text{ion},f} a_{\text{prop},f}$  can be replaced by the continuum electron wave packet obtained, e.g. from the time-dependent Schrödinger equation (TDSE) or the strong-field approximation [22]. We use  $a_{\text{ion},f} \propto \sqrt{I_f}$  with  $I_f$  the strong-field ionization rate to the cation state  $f$ . A possible ionization phase is neglected, which is justified by static tunneling considerations [23] and confirmed for simple systems by measurements of the vanishing tunneling delay time [24]. For the phase accumulated during the propagation of the electron in the laser field, we use  $a_{\text{prop},f} \propto e^{-iI_p f \tau}$ , where  $I_p f$  is the vertical ionization potential associated with the cation state  $f$  and  $\tau$  is the transit time of the electron in the continuum,  $\tau \approx 0.8 - 1.7$  fs in a laser pulse centered at 800 nm [25,26].

We now describe high-harmonic emission from a photoexcited molecular system. Photoexcitation prepares a molecule in a superposition state  $\Psi(\mathbf{r}, \mathbf{R}, t)$  of the unexcited ground state and a set of electronically excited states  $i$ . The total wave function can be written in terms of a sum of products of electronic wave functions  $\phi$  and nuclear wave functions  $\chi$

$$\Psi(\mathbf{r}, \mathbf{R}, t) = c_g(t) \phi_g(\mathbf{r}; \mathbf{R}) \chi_g(\mathbf{R}) + \sum_i c_i(t) \phi_i(\mathbf{r}; \mathbf{R}) \chi_i(\mathbf{R}, t), \quad (2)$$

where  $\mathbf{r}$  and  $\mathbf{R}$  represent the electronic and nuclear coordinates, respectively, and  $t$  the time elapsed since photoexcitation. The excited state fraction can be defined by the coefficients of the superposition state as  $r = 1 - |c_g|^2 = \sum_i |c_i|^2$  and  $|c_i|^2 = r_i$ . Then, the high-harmonic electric field emitted by this superposition state is given by a coherent sum of the XUV radiation emitted from the different electronic states

$$E_{\text{XUV}}(\Omega, t) = (1 - r(t)) \tilde{d}_g(\Omega) + \sum_i r_i(t) \tilde{d}_i(\Omega, t), \quad (3)$$

where  $\tilde{d}_i(\Omega, t)$  is the complex spectral representation of high-harmonic emission at photon frequency  $\Omega$  for the neutral molecular

wave packet in the electronic state  $i$ . The emission terms in Eq. (3) all correspond to ionization from and recombination to the same electronic states.

Expression (3) would thus be identical for an incoherent mixture of molecules in the prepared states. However, in principle, cross terms can also occur, i.e. high-harmonic emission from pathways, in which the continuum electron recombines to a different state than the one it was ionized from. As shown in Ref. [18] (supplementary material), these cross terms are proportional to the overlap integrals of the nuclear wave functions  $\langle \chi_g | \chi_i \rangle$ . In cases of simple adiabatic photodissociation, these overlap integrals will decay towards zero rapidly, but in other cases they may not. The corresponding hyper-Raman-like transitions induced by the strong laser field would emit frequencies that are most readily predicted using the principles of conservation of momentum, energy and parity discussed in Ref. [27]. The one-photon absorption to the “bright state”  $e$  at photon frequency  $\omega_{ge}$  changes the total parity of the molecular wave function. A cross-term corresponding to ionization from the excited state  $e$  and recombination to  $g$  would thus emit photon frequencies according to

$$\Omega = \omega_{ge} + 2n\omega, \quad (4)$$

with  $n$  integer and  $\omega$  the fundamental photon frequency. Cross-terms among the different excited electronic states  $i$  would emit regular odd harmonics if the states have the same parity and even harmonics if the states have opposite parities. In the photochemical dynamics of  $\text{Br}_2$  and  $\text{NO}_2$ , prepared by photoexcitation at 400 nm, which will be further discussed below, the cross-term between the excited and ground states would thus emit even harmonics. The emission from this cross term unfortunately coincides spectrally with cross-correlation signal obtained from wave-mixing in the transient grating geometry as discussed below [27] and could thus not be clearly identified. We therefore restrict our analysis to Eq. (3).

In general, photochemical dynamics occur on intersecting potential energy surfaces and the choice of an adequate representation of the electronic states is essential. The most natural choice is a set of diabatic electronic states because their electronic character varies slowly with nuclear coordinates, even in the vicinity of intersections, and will thus allow a simpler formulation of the high-harmonic generation process. The complex spectral components of high-harmonic emission will thus be calculated for each wave packet in a diabatic electronic state as

$$\tilde{d}_i(\Omega, t) = \int d\mathbf{R} |\chi_i(\mathbf{R}, t)|^2 \sum_f \sqrt{I_f^{\text{if}}(\mathbf{R})} e^{-iI_p^{\text{if}}(\mathbf{R})\tau} d_r^{\text{if}}(\mathbf{R}), \quad (5)$$

where the sum runs over the accessible states  $f$  of the cation.  $I_f^{\text{if}}$  is the rate of strong-field ionization from the neutral state  $i$  to the cation state  $f$ ,  $I_p^{\text{if}}$  the corresponding vertical ionization potential and  $d_r^{\text{if}}$  the corresponding molecular-frame complex photorecombination matrix element. The  $e^{-iI_p^{\text{if}}(\mathbf{R})\tau}$  phase term is an approximation of the propagation phase and is dominated by the nuclear coordinate-dependent and thus time-dependent ionization potential [25,26]. This approximation is good when  $\Omega \gg I_p$ . We note that the electron transit time  $\tau$  in the continuum is slightly different when two electronic states with different  $I_p$  emit harmonics at the same photon frequency  $\Omega$ . Thus,  $\tau$  in Eq. (5) is an average of the transit times associated with state  $i$  and the ground state [26].

The ionization rates can be calculated analytically in many different ways (see e.g. Refs. [28,29]) or by solving the TDSE for a single electron in the ionic Hartree potential of the corresponding state of the cation [30]. The photorecombination dipoles, which contain the amplitude and phase contributions of the recombination step of HHG, are calculated using quantum scattering calculations in the potential of the cation state  $f$  [20,22,31]. The

nuclear-coordinate dependence of the ionization potential as well as the potentials for solving the TDSE or quantum scattering problems are obtained from *ab initio* quantum chemistry. We note that the choice of a diabatic electronic basis, which causes the electronic character of the states to vary slowly with nuclear coordinates, implies that the potential energy surfaces obtained from quantum chemical calculations need to be “diabatized” before they are used to calculate the quantities discussed above.

## 2.2. Relation to photoelectron spectroscopy

The photoionization of a fixed-in-space molecule contains information on the electronic structure of the molecule in the angular distribution of the photoelectrons. The angular distribution can be described in terms of a doubly-differential photoionization cross section [22,32]

$$\frac{d^2\sigma^I}{d\Omega_{\mathbf{k}}d\Omega_{\mathbf{n}}} = \frac{4\pi^2\omega k}{c} \left| d_{\mathbf{k},\mathbf{n}}^-(\Omega) \right|^2, \quad (6)$$

where  $\mathbf{n}$  is the direction of the linear polarization of the photoionizing radiation and  $\mathbf{k}$  is the momentum of the photoelectron. The photorecombination matrix element is the complex conjugate of the photoionization matrix element  $d_{\mathbf{k},\mathbf{n}}^+ = d_{\mathbf{k},\mathbf{n}}^{*-}$  and is the complex quantity that enters Eq. (5) as  $d_i^f$ . For completeness, we note that the photorecombination matrix element is related to the differential photorecombination cross section by

$$\frac{d^2\sigma^R}{d\Omega_{\mathbf{k}}d\Omega_{\mathbf{n}}} = \frac{4\pi^2\omega^3}{c^3k} \left| d_{\mathbf{k},\mathbf{n}}^+(\Omega) \right|^2. \quad (7)$$

The fact that angular distributions in photoionization and photorecombination in high-harmonic generation are described by mutually complex conjugated matrix elements, comes from the boundary conditions imposed in describing the problem. An angular distribution is calculated by matching the outgoing photoelectron wave to a plane wave (or Coulomb wave) of momentum  $\mathbf{k}$  on the detector [33]. The photorecombination in HHG is described by a photoelectron returning into the molecular potential as a plane wave (or Coulomb wave) with an asymptotic momentum  $\mathbf{k}$  which then scatters in the molecular potential before photorecombination. Describing the latter step in HHG with  $d_{\mathbf{k},\mathbf{n}}^+(\Omega)$  thus contains at least two implicit approximations: (i) the effect of the laser field on the cation can be neglected during photorecombination and (ii) the photoelectron has travelled far enough in the laser field, that it can be approximated as a plane wave (or Coulomb wave) at the outer turning point of its trajectory. The first assumption has been verified in rare gas atoms [20,34,35] and in a range of small molecules [22,23,31,36] but must be carefully checked in larger molecules in the future. The second assumption is probably reasonable since typical excursion amplitudes in an 800 nm laser field are in the range of 5–10 Å for the short electron trajectories that are usually detected. This is likely to be sufficient to escape from the short-range potential of small molecular cations, but the effect of the Coulomb potential may need to be considered in the future.

The most attractive aspect of using photoionization theory in HHG is that many complex multielectron effects can be absorbed into the photorecombination matrix element using well established methods. This includes such important effects as recollision-induced photoexcitation of the molecular cation prior to recombination and exchange and correlation effects [35,37]. A very successful description of photoionization processes in molecules is given by multichannel-quantum defect theory [38] which we anticipate to become an important addition to current theoretical models of HHG. Photoionization cross sections are highly structured in the vicinity of photoionization thresholds due to high Rydberg states which are strongly coupled to the accessible continua

through electronic, vibrational and rotational interactions. These sharp structures do of course not show up in HHG, because of temporal filtering in the HHG emission process which has to be accounted for when detailed comparisons are made [39].

The main difference between HHG and photoelectron spectroscopy (PES) comes from the coherence properties of HHG. Photoionization transitions connect an initial state with a set of final continuum states which are orthogonal to each other. Hence interference will only be present in photoionization if the coherent bandwidth of the photoionization source covers more than one final state of the cation [40] and the continuum electrons associated with those states of the cation share at least one irreducible representation. This situation is different in HHG for two reasons: (i) the relevant bandwidth is not that of the light source driving the process but that of the recombining photoelectron wave packet generated by strong-field ionization and (ii) electromagnetic interference takes place between all possible HHG emission channels because photons are detected. This means (i) that HHG can probe attosecond dynamics occurring between ionization and recombination [23,36,41] and (ii) that it is highly sensitive to weak emission channels, what we will refer to as “homodyne advantage”.

## 3. Experimental section

### 3.1. Collinear pump–probe experiments

The coherent nature of high-harmonic emission allows the unexcited molecules to act as local oscillators against which the dynamics of the excited molecules are observed [17,18]. In a collinear pump–probe experiment, as reported in Ref. [17], the total electric field of high-harmonic emission can be written as a sum of contributions from the electronic ground state ( $g$ ) and the excited states ( $i$ ) as given in Eq. (3). The measured high-harmonic intensity at photon frequency  $\Omega$  will thus be given by

$$I_{\text{UV}}(\Omega, t) = \left| (1 - r(t))\tilde{d}_g(\Omega) + \sum_i r_i(t)\tilde{d}_i(\Omega, t) \right|^2. \quad (8)$$

The signal is thus a coherent sum of emissions from the electronic states populated during the photochemical process, which is particularly sensitive to emission from weakly populated states, and to phase shifts between the emission from different states. When the intensity of the exciting pulse is kept low, the ground state molecules can be considered to be static, hence  $\tilde{d}_g(\Omega)$  does not depend on the pump–probe delay time  $t$ . When the pump pulse becomes intense, dynamics can also be prepared in the electronic ground state, which has been described in Ref. [18].

In the signal described by Eq. (8), temporal variations can be caused by variations of the populations  $r_i(t)$  or the amplitude or phase of  $d_i(\Omega, t)$ . This ambiguity can be partially resolved by replacing the collinear excitation with a transient grating geometry. The transient grating has been first applied to HHG in Ref. [42] in the context of rotational alignment and in Ref. [18] in the context of single-photon excitation.

### 3.2. Transient grating spectroscopy with single-photon excitation

Experimentally, a transient grating of photoexcitation is realized by crossing two synchronized laser beams, resonant with the molecular transition, in a supersonic expansion as shown in Fig. 1. The interference between the two beams creates alternating planes of excited and unexcited molecules along the vertical ( $x$ ) direction. This structured sample is then probed by HHG of an intense infrared pulse propagating along the horizontal direction ( $y$ ). The high harmonics are then spectrally dispersed in the  $yz$ -plane by a concave grating, while the beam freely diverges in the  $x$ -direction. This

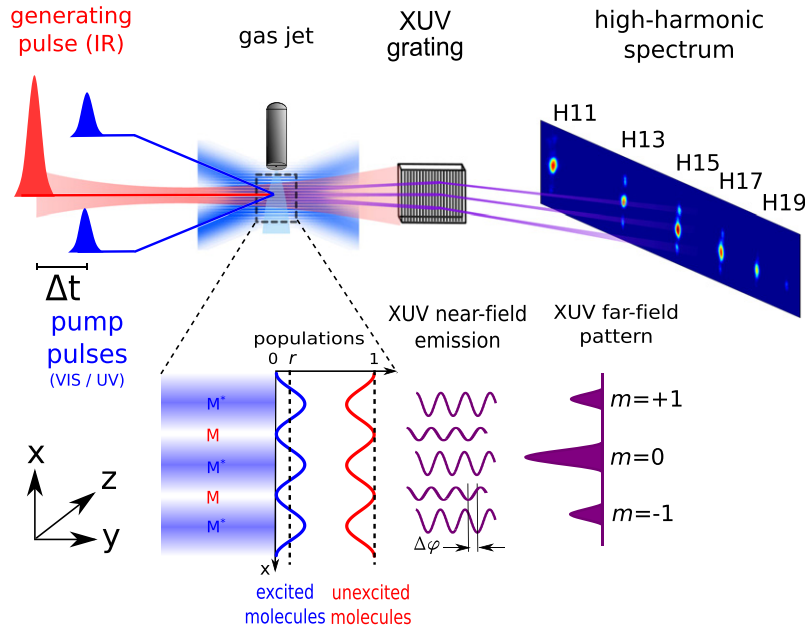


**Fig. 1.** Experimental setup for high-harmonic generation in a transient grating geometry. A spatially modulated population of excited molecules is created by the transient grating through single-photon absorption. The spectrum is dispersed by an XUV grating in the horizontal direction. The periodic structure of the transient grating of the transient grating gives rise to a modulation of the high-harmonic amplitudes and phases in the near field, which is translated to vertically separated first-order diffraction in the far field.

results in the observation of a high-harmonic spectrum in the horizontal  $yz$ -plane, which will be referred to as the “non-diffracted” component, and diffraction orders appearing at vertically displaced positions above and below each harmonic order.

The intensity distribution along the  $x$ -direction of the transient grating can be described by

$$I(x) = I_{av}(\cos(kx) + 1), \quad (9)$$

where  $k = 2\pi/\Lambda$ ,  $\Lambda$  is the spatial period of the grating determined by the crossing angle and wavelength of the pump beams, and  $I_{av}$  is the average of the pump intensity over the dimension  $x$ . One-photon excitation of the molecules in the ground state (g) transfers a fraction of the molecules into an excited state (e). Consequently, the excited state fraction is also modulated spatially according to

$$r(x) = r(\cos(kx) + 1), \quad (10)$$

where  $r$  is the excited state fraction averaged over  $x$ , which is determined from the measured pulse intensity, focal spot sizes and known photoabsorption cross sections.

The spectrally dispersed far-field profile of the high harmonics, which is observed on the detector, is given by the Fourier transform of the near-field modulation of the XUV field at the exit of the grating. Inserting the spatial modulation of the excited state fraction from Eq. (10) into the expression of the total electric field in Eq. (3) and Fourier-transforming the expression gives

$$FT_{x \rightarrow \xi}(E_{XUV}(\Omega, t, x)) = \left( (1-r(t))\tilde{d}_g(\Omega) + \sum_i r_i(t)\tilde{d}_i(\Omega, t) \right) \delta(\xi) + \frac{1}{2} \left( \sum_i r_i(t)(\tilde{d}_i(\Omega, t) - \tilde{d}_g(\Omega)) \right) \left( \delta\left(\xi - \frac{k}{2\pi}\right) + \delta\left(\xi + \frac{k}{2\pi}\right) \right) \quad (11)$$

where  $\xi$  is the spatial  $x$ -direction frequency at the exit of the grating which translates into a diffraction angle upon propagation. This yields the intensity of the non-diffracted and diffracted radiation that arrive vertically displaced at the detector,

$$I_{m=0}(\Omega, t) = \left| (1-r(t))\tilde{d}_g(\Omega) + \sum_i r_i(t)\tilde{d}_i(\Omega, t) \right|^2 \quad (12)$$

$$I_{m=\pm 1}(\Omega, t) = \frac{1}{4} \left| \sum_i r_i(t)(\tilde{d}_i(\Omega, t) - \tilde{d}_g(\Omega)) \right|^2. \quad (13)$$

Notably, only first order diffraction is obtained. Higher-order diffraction will appear if the excitation grating deviates from a sinusoidal function which can occur when single-photon excitation reaches saturation or multiphoton excitation takes place. We note that the non-diffracted intensity  $I_{m=0}$  is the same as what would be observed in a collinear pump-probe measurement (see Eq. (8)), i.e. the interference between the emissions from the ground and excited states weighted by their populations. However, the diffracted intensity  $I_{m=\pm 1}$  is generated by interference between the emissions of excited and unexcited molecules with equal weights.

This property can be intuitively understood from Fig. 1. The grating of excited molecules is accompanied by a grating of opposite amplitude in the ground state population. The consequence is that the first order diffraction peaks in the far field record the emission from a 1:1 interference of excited and unexcited molecules, whereas the non-diffracted signal records the spatial average of the emission which is weighted by the populations. Thus, the signal in  $m=1$  has an enhanced sensitivity to the signal emitted by the electronically excited state, whereas the signal in  $m=0$  is identical to what would be observed in a collinear experiment. This is the reason why the expressions in Eqs. (12) and (8) are identical when  $r$  and  $r_i$  are interpreted as the spatially averaged excited state fractions.

A frequent case in polyatomic molecules, that will also be further discussed below in relation to the  $\text{NO}_2$  experiments, is that the quantities  $\tilde{d}_i(\Omega, t)$  vary only over a short time interval and then reach nearly stationary values. In this case, the temporal variations of  $I_{m=0}$  and  $I_{m=\pm 1}$  will mostly reflect population transfers between the excited diabatic electronic states  $i$ . In diatomic molecules and in polyatomic molecules with a single soft coordinate, the nuclear wave packet will remain relatively confined in configuration space and in such a case, the temporal variation of  $\tilde{d}_i(\Omega, t)$  will dominate the observed dynamics. When a single excited state is populated, as e.g. in the example of  $\text{Br}_2$  discussed below, the information contained in the intensities  $I_{m=0}$  and  $I_{m=\pm 1}$  is sufficient to reconstruct simultaneously both the high-harmonic amplitudes and phases of the excited state relative to the ground state [18]. The corresponding procedure is described in the supplementary material of Ref. [18]. We note that this inversion is still applicable when

strong-field ionization to multiple states of the cation takes place (i.e. multiple orbitals are ionized) from the ground state and/or the excited state. In this case, the procedure determines the amplitudes and phases of  $\tilde{d}_i(\Omega, t)$  in the sense of Eq. (5), where the sum runs over all accessible states  $f$  of the cation. We note that this is even true in the most general case when the ground and excited states ionize to distinct sets of cation states.

### 3.3. Spectrally resolved far-field high-harmonic signals

The spectrally resolved far-field high-harmonic signals obtained in a transient grating experiment using 400 nm pump pulses and an 800 nm probe pulse are shown in Fig. 2. This particular data set comes from an experiment performed in NO<sub>2</sub> [19] but the observed pattern is qualitatively independent of the probed molecule (except for the value of the cut-off photon energy). Fig. 2a was recorded with the probe pulse preceding the pump pulses and shows the normal odd harmonic orders. Fig. 2b was recorded at temporal overlap and shows, in addition to the odd harmonics, two intensity spots at each even-harmonic position which are vertically displaced relative to the odd harmonics. In addition, one spot is also observed above and below each odd harmonic order. Finally, Fig. 2c was recorded with the probe pulse following the pump pulses and shows only the additional spots above and below each harmonic order.

The off-axis intensity contributions in Fig. 2c are the first-order diffraction spots  $m = \pm 1$  described in the last section. Diffraction is of course only observed when the molecule is excited by the 400 nm pump pulse. The pattern observed in Fig. 2b is dominated by wave mixing between the 400 nm pump and 800 nm probe pulses. As described in Ref. [27], a non-collinear arrangement of strong 800 nm and weak 400 nm laser beams generates off-axis high-harmonic emission at odd as well as even harmonic orders of the 800 nm field. The photon energy of all observed emission spots must correspond to an odd total number of photons. Momentum conservation, i.e. the addition of the momentum vectors of all photons contributing to a given order, determines the position of the harmonics on the detector. These multiphoton processes result in ultra-high-order wave mixing of  $n_1$  photons contributed by the strong field and  $n_2$  photons contributed by the weak field. This process can be explained in terms of perturbative non-linear optics with respect to the weak field. This means that the harmonic signal follows an  $I_2^{n_2}$  scaling law, where  $I_2$  is the weak-field (400 nm) intensity and  $n_2$  is the number of photons of the weak field participating in the process. The odd off-axis harmonics correspond to two-photon processes in the 400 nm field and the harmonic signal scales with  $I_2^2$ . For example, the observed off-axis harmonics observed in Fig. 2b at the photon energy of H13 correspond to an  $n_1 = 9$  and  $n_2 = 2$  process. The even-order off-axis harmonics correspond to single-photon processes in the 400 nm field, i.e. H12 is generated by an  $n_1 = 10$  and  $n_2 = 1$  process. Since two 400 nm

beams are present in the transient grating, whereas only one was used in Ref. [27], the features described in the last two sentences can also be produced by  $n_1 = 17, n_2 = -2$  and  $n_1 = 14$  and  $n_2 = -1$  processes, respectively, but their contributions are significantly weaker than those corresponding to the additive combinations [27].

We thus find that the signal from wave-mixing involving two photons of 400 nm wavelength at temporal overlap of pump and probe pulses spatially overlaps with the diffracted signal from the transient grating. The energy scaling of wave mixing follows  $I_2^2$ , which is identical to the scaling of the diffracted signal because of its  $r^2$ -dependence (Eq. (13)). The two processes can thus not be easily distinguished. However, wave mixing is much less efficient for perpendicularly polarized pulses than for parallel ones as we will discuss below [27].

## 4. Discussion of results on the photodissociation of Br<sub>2</sub> molecules

We first discuss the results obtained on the photodissociation of Br<sub>2</sub> [17,18]. The relevant potential energy curves of Br<sub>2</sub> and Br<sub>2</sub><sup>+</sup> are shown in Fig. 3. Single-photon excitation from the X <sup>1</sup>Σ<sub>g</sub><sup>+</sup> ground state at 400 nm prepares a wave packet in the repulsive C <sup>1</sup>Π<sub>1u</sub> excited state. After dissociation, the bromine atoms are in the <sup>2</sup>P<sub>3/2</sub>,  $|m_j| = 1/2$  state [44], showing that dissociation proceeds fully adiabatically although the C-state curve crosses that of the B state. The electronically excited molecules in the C <sup>1</sup>Π<sub>1u</sub> state are then probed by HHG against the molecules in the ground state, which act as local oscillators. Tunnel ionization, the first step in HHG, occurs predominantly to the X<sup>+</sup> <sup>2</sup>Π<sub>g</sub> ground state of Br<sub>2</sub><sup>+</sup>. Photoexcitation decreases the ionization potential and thus increases the ionization yield relative to the ground state as observed in Ref. [17]. The ionization potential of the excited-state wave packet, which depends on the internuclear separation, thus changes with the pump-probe delay, which manifests itself in a varying phase contribution to Eq. (5). Recombination, the third step in HHG, will occur to the same state from which the molecule was ionized. After photoexcitation, the excited state nuclear wave packet has a significant extension along the internuclear separation coordinate (approximately 1.5 Å FWHM) which does not significantly increase over the first 200 fs. As we will show next, this extension plays an important role for calculating the propagation phase and thus crucially affects the nature of the observed spectral interferences.

Fig. 4 shows the variation of the intensities  $I_{m=0}$  and  $I_{m=1}$  for harmonic orders 13–21. The data has been recorded in a transient grating formed by two 400 nm pump laser pulses and probed by an 800 nm laser pulse generating high harmonics. The main observation for  $m = 0$  is the initial decrease of the harmonic signal after excitation and the subsequent increase to an asymptotic level depending on the harmonic order. In  $m = 1$  the signals increase

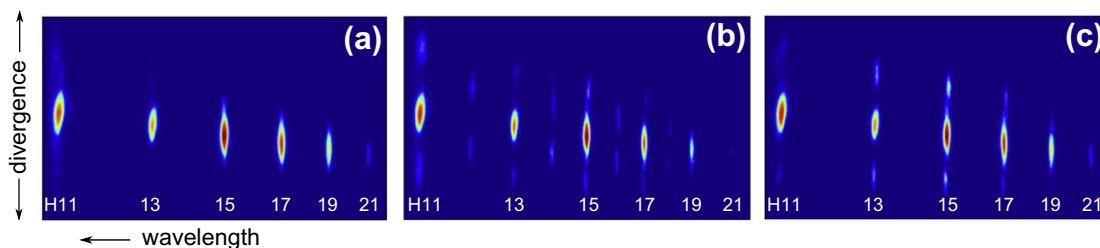
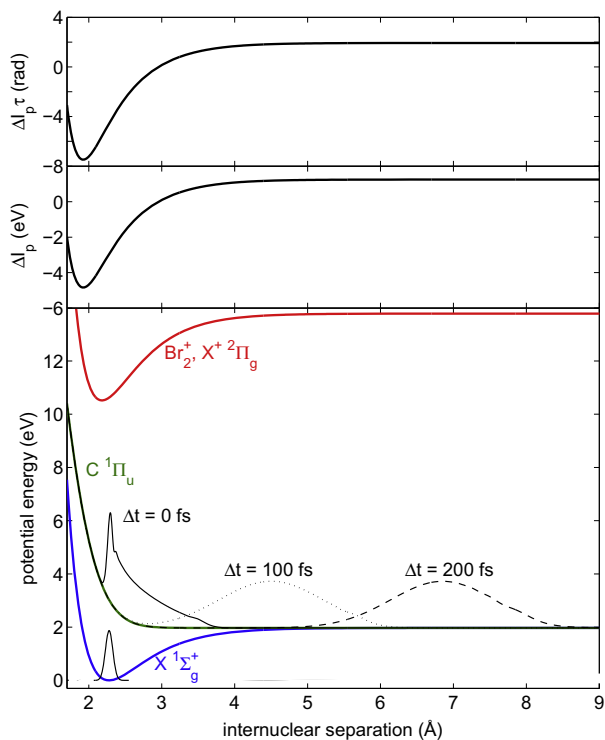


Fig. 2. Spectrally dispersed far-field profile of high harmonics observed in a transient grating experiment with NO<sub>2</sub> [19]. Panels a, b and c correspond to negative, zero and positive delays between the 400 nm transient grating pump pulses and the 800 nm high-harmonic generating probe pulse.



**Fig. 3.** Potential energy curves of the  $X^1\Sigma_g^+$  ground state and the repulsive  $C^1\Pi_u$  excited state of  $\text{Br}_2$  as well as the  $X^+2\Pi_g$  ground state of  $\text{Br}_2^+$ . The nuclear wave packet on the repulsive  $C^1\Pi_u$  state after excitation in the transient grating is shown for selected time delays. The difference in the ionization potentials between ionization from the  $X^1\Sigma_g^+$  ground state and the  $C^1\Pi_u$  excited state is shown in the central panel. The corresponding propagation phase  $\Delta I_p\tau$  for  $\tau = 1$  fs is shown in the upper panel.

after excitation, then decrease and subsequently increase to their asymptotic levels. This asymptotic level is non-zero because, at long delays, the transient grating consists of alternating planes of atoms and molecules which emit high harmonics with different phases and amplitudes.

Here, we will focus on the comparison of the pump–probe data shown in Fig. 4 with model calculations. We simulate the spectra using a simple model introduced in Ref. [17], where it was

compared to data from a collinear pump–probe experiment. Here, we use Eqs. (12) and (13) to calculate the high-harmonic intensities in  $m = 0$  and  $m = 1$ . The sum in these equations is simplified to one term, since a single electronically excited state is prepared. To study the effect of the propagation phase term, we neglect the variation of the ionization rate with internuclear separation and model the recombination matrix elements of the excited molecules as a smoothed step function (the error function) that increases from 1 to 2, reflecting the increase from one to two emitters during dissociation. Photodissociation is modeled by propagating a wave packet created by a 40 fs excitation pulse centered at 400 nm, on the  $C^1\Pi_u$  dissociative potential energy curve taken from [45] using the split operator technique [43]. The intensity of the excitation pulse is chosen to yield an excited state fraction of  $r = 0.14$ . The phase terms needed in Eqs. (12) and (13) are evaluated using the strong-field approximation [25]. Classical simulations of the electron trajectories yield the ionization and recombination times and thus the transit times of the continuum electrons associated with each harmonic order. The results of these calculations are shown in Fig. 5.

From comparing the experimental and theoretical data it can be seen that this extremely simplified model reproduces the main observations of the initial decrease (increase) in the non-diffracted (diffracted) signal. Since the variation of the ionization rate was neglected in the calculations and the recombination amplitude has been modeled as a simple step function, the calculated modulations can only result from the interferences caused by the propagation phase and thus from the difference in the ionization potentials between the excited and ground states, which varies rapidly during the first tens of femtoseconds after excitation as can be seen in Fig. 3. Note that the large observed local maximum at zero pump–probe delay in the diffracted signal is dominated by wave mixing as discussed in Section 3.3 and is thus not present in the simulations. To highlight the effect of the wave packet extension on the role of the phase contribution, we compute the latter in two different ways. A simple and naive approach is to calculate the phase exponential  $e^{-i(\Delta I_p)\tau}$  of the normalized intensities by taking an ionization potential  $\langle \Delta I_p \rangle = \langle \chi_e | I_{p,e}(R) - I_{p,g} | \chi_e \rangle$  averaged over the nuclear wave packet in the excited state. The R-dependences of these quantities are shown in the central (ionization potential difference  $\Delta I_p$ ) and upper panel (corresponding phase  $\Delta I_p\tau$  for  $\tau = 1.0$  fs) of Fig. 3. However, this approach neglects the significant extension of the wave packet in coordinate space. The correct way

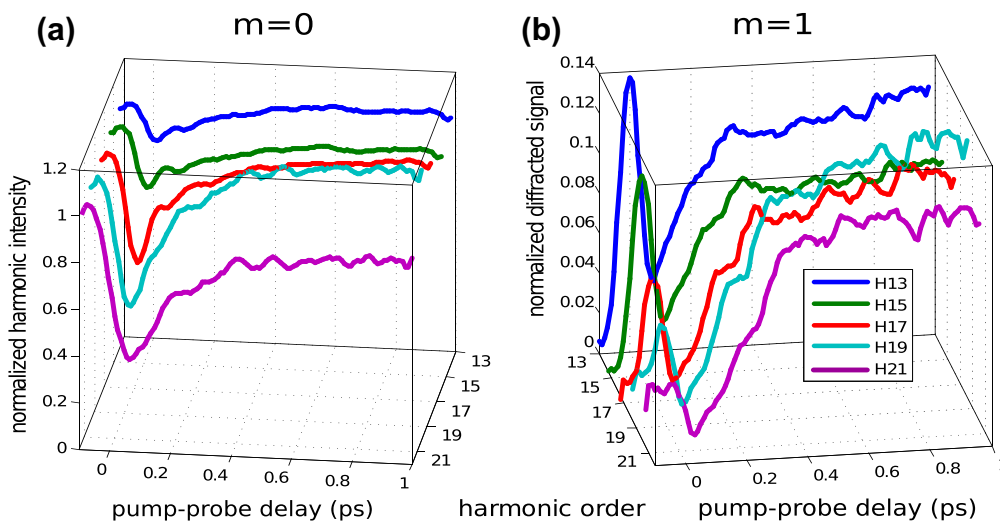


**Fig. 4.** Temporal evolution of the high-harmonic intensities measured in  $\text{Br}_2$  for the harmonic orders 13–21 for the (a) zero-order and (b) first-order diffraction signals. Pump and probe pulses are polarized parallel to each other. All signals have been normalized to the non-diffracted intensity at negative pump–probe delays in each harmonic order. The experimental data is taken from Ref. [18].

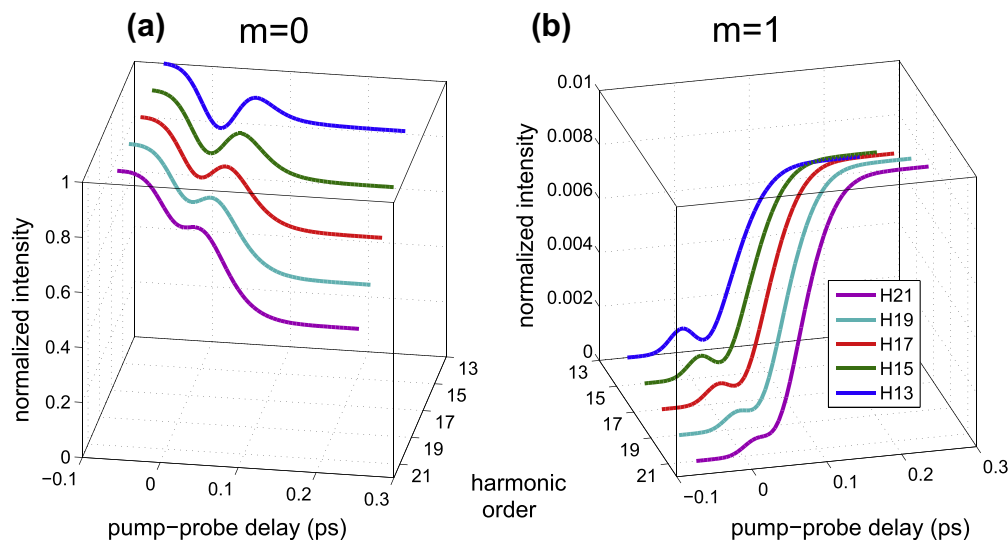


Fig. 5. Calculated temporal evolution of the harmonic intensities in Br<sub>2</sub> for harmonics 13–21 for the (a) zero-order and (b) first-order diffraction signal.

of calculating the propagation phase term is to average the exponential over the wave packet, i.e. taking the exponential propagation phase term as  $\langle e^{-i\Delta I_p(R)\tau} \rangle = \langle \chi_e | e^{-i\Delta I_p(R)\tau} | \chi_e \rangle$ . In a semi-classical interpretation, this way of calculating the phase term corresponds to allowing interference between the emissions of an ensemble of molecules with different internuclear separations.

To demonstrate the effect of the wave packet width, the intensities of H15 are calculated with the propagation phase term obtained in either of the two ways described above and is shown in the lower panels of Fig. 6. The amplitude and phase of the propagation phase terms are shown in the upper panels. The harmonic signal shows a similar oscillatory behavior in both cases. However, the oscillations in the harmonic signal are much less pronounced for the case of a  $\langle e^{-i\Delta I_p(R)\tau} \rangle$  propagation term (right-hand side), which is closer to the experimental results. In both cases the propagation phases show the same asymptotic behavior, i.e. they vary from about +4 rad to –2 rad. However, the phase term averaged over the wave packet ( $e^{-i\Delta I_p(R)\tau}$ ) leads to a steeper decrease of the phase after excitation, causing destructive interference as indicated by the deep minimum in the amplitude. This means that high-harmonic emission from the excited state itself is strongly suppressed for early delay times as a consequence of the steep variation of the ionization potential combined with the large spatial extension of the wave packet. This self-interference is neglected when an averaged value of the is used  $I_p$  instead of the averaged phase term.

Further effects that are important in explaining the evolution of the harmonic signal are the interference of the emission from the excited state with that of the ground state. This interference is mainly destructive as shown in Ref. [17], where the harmonic signal and the total ion yield were found to modulate in opposite directions. After excitation, the ion yield increases due to a higher ionization rate of the excited state, which should normally cause an increase of the harmonic signal. But instead, a decrease of the high-harmonic signal was observed. Thus it can be concluded that the first minimum in the time evolution of the non-diffracted harmonic signal seen in the experiments (Fig. 4) as well as in our simulations (Fig. 5) is also caused by the interference of harmonics from excited and unexcited molecules, while the self-interference of the evolving excited state wave packet prevents an even deeper modulation of the signal.

What has been neglected in this discussion so far is the variation of the photorecombination matrix elements with internuclear

separation. In the adiabatic photodissociation of diatomic molecules, this variation is dominated by two-center interference. This concept originated in photoionization [46], where it was observed recently [47]. It has been extensively discussed in high-harmonic generation [48], where it has been associated with plane-wave descriptions of the continuum. However, two-center interference is also predicted in quantitative scattering calculations [22] and observed in recent experiments [49], showing its occurrence in real molecules.

As we do not use quantitative recombination dipoles in this study, two-center interference is not contained in our simple model. However, the reconstruction of high-harmonic amplitudes in Ref. [18] revealed distinct minima appearing at different times in different harmonic orders. The observed minima spanned the range 51–78 fs (for harmonics 21–13) and are in quantitative agreement with the wave packet calculations discussed above, as shown in Ref. [50]. These minima are thus caused by the increasing internuclear separation of the molecule, where the de-Broglie wavelength  $\lambda_e$  of the recombining photoelectron fulfills a destructive interference condition with respect to the electron–hole wavefunction of the dissociating molecule. Destructive interference occurs for internuclear separations meeting the condition  $R = (2n + 1)/2\lambda_e$  for a wave function of ungerade symmetry ( $n = 1$  in the present case). For higher values of  $n$  further minima could be expected. However, they are absent, which illustrates the transition from molecular to atomic character of high-harmonic generation, or, equivalently, the fact that all 4 molecular orbitals of the valence shell ( $\sigma_g, \pi_u, \pi_g, \sigma_u$ ) become degenerate when the molecule dissociates [51].

## 5. Discussion of results on the non-adiabatic dynamics in NO<sub>2</sub> molecules

We now turn to NO<sub>2</sub>, which is a very interesting molecule from a photochemical point of view due to the conical intersection of its first electronically excited state  $\tilde{A}^2B_2$  with the ground state  $\tilde{X}^2A_1$ . The intersection of two potential energy surfaces is associated with strong coupling of the nuclear and electronic dynamics thus inducing highly non-adiabatic behavior [52–55]. Here, we are mostly interested in probing the electronic dynamics associated with this non-adiabatic phenomenon, namely the crossing of the conical intersection from an electronic point of view. The relevant poten-

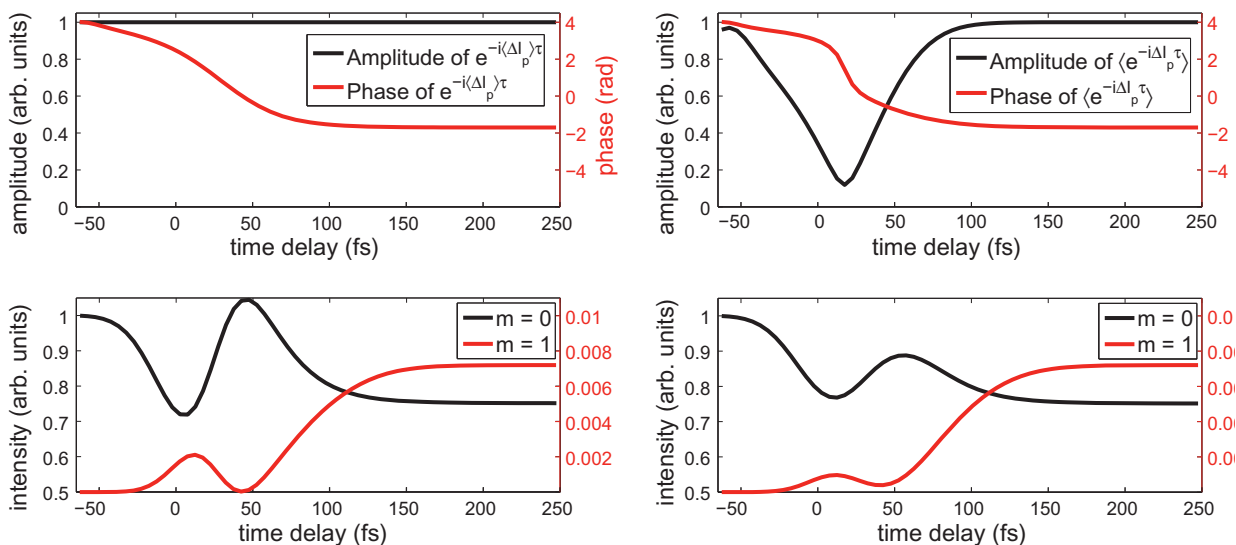


**Fig. 6.** Lower panel: Calculated temporal evolution of H15 in Br<sub>2</sub> for the non-diffracted and first-order diffraction signals. The calculation was performed either by computing the phase with the ionization potential corresponding to the expectation value of the internuclear separation at a certain time delay (i.e. as  $e^{-i\langle \Delta I_p \rangle \tau}$ , left hand side,  $\tau = 0.89$  fs) or by averaging the exponential phase term over the wave packet (i.e. by taking the propagation term  $\langle \chi_e | e^{-i\Delta I_p \tau} | \chi_e \rangle$ , right hand side,  $\tau = 0.89$  fs). The propagation phase terms are shown in the respective upper panels, in terms of their amplitude and phase.

tial energy surfaces along the bending coordinate  $\beta$  are shown in Fig. 7. The electronic ground state  $\tilde{X}^2A_1$  possesses a  $(\dots)(b_2)^2(a_1)^1$  configuration. By excitation with a 40 fs pulse centered at 401 nm (spectral FWHM of 5 nm) population is transferred to the  $\tilde{A}^2B_2$  state with a  $(\dots)(b_2)^1(a_1)^2$  configuration. The conical intersection visible in the figure as crossing of the potential energy surfaces along the bending coordinate, is actually part of a one-dimensional seam of conical intersections spanning the symmetric stretching coordinate. The propagating wave packet is sketched with an underestimated width and will be discussed below. In addition, the relevant cationic surfaces are shown.

In the following we consider which states of the cation are involved during HHG, since this is important in interpreting the experimental results. The transition dipole moment of the  $\tilde{A}^2B_2 \leftarrow \tilde{X}^2A_1$  transition lies parallel to the y-axis (O–O axis). Thus, excited molecules have their y-axis preferentially aligned parallel to the polarization of the pump pulse. In the case of perpendicular polarizations of the pump and probe pulses, ionization occurs preferentially from the  $a_1$  orbital because of its large lobe along the z-axis. Ionization from the  $b_2$  orbital is suppressed along this direction by the presence of a nodal plane. The ionization propensities of these two orbitals are reversed when the probe pulse polarization is parallel to the y-axis. Thus, for perpendicular polarizations, molecules in the ground state will ionize to the  $^1A_1$  state of the cation (XS channel, X represents the neutral ground state, S the singlet state of the cation), whereas molecules in the excited state ionize to the  $^3B_2$  cationic state (AT channel, A represents the electronically excited state, T the triplet state of the cation). In the case of parallel

potential energy surfaces of the relevant electronic states of NO<sub>2</sub> and NO<sub>2</sub><sup>+</sup> as function of the bending angle. The HOMO and HOMO-1 orbitals computed on the Hartree-Fock level as well as the pump-pulse polarization are shown on top right. The temporal evolution of the population in the diabatic A and X states are shown in the lower right-hand panel. The latter are taken from 3D wave packet calculations using a 40-fs pump pulse centered at 400 nm [56].

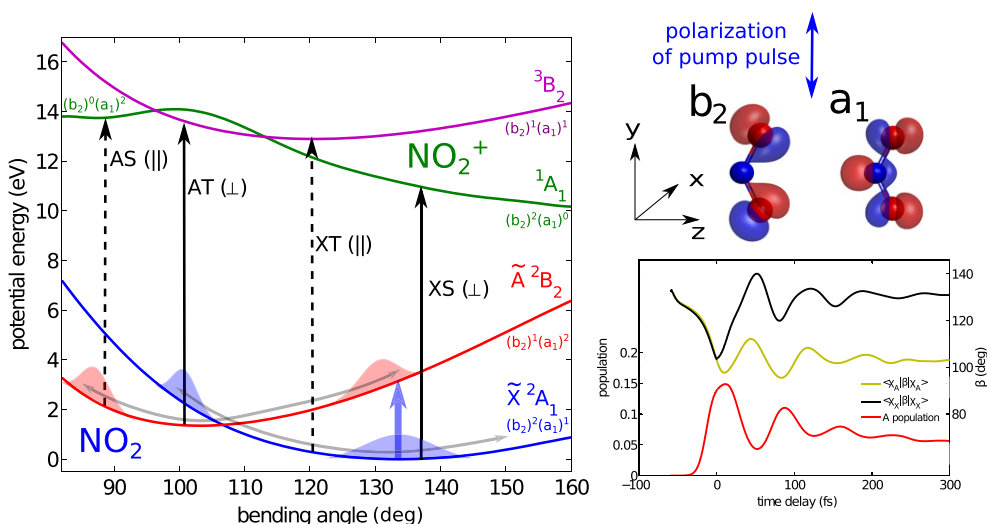


**Fig. 7.** Potential energy surfaces of the relevant electronic states of NO<sub>2</sub> and NO<sub>2</sub><sup>+</sup> as function of the bending angle. The HOMO and HOMO-1 orbitals computed on the Hartree-Fock level as well as the pump-pulse polarization are shown on top right. The temporal evolution of the population in the diabatic A and X states are shown in the lower right-hand panel. The latter are taken from 3D wave packet calculations using a 40-fs pump pulse centered at 400 nm [56].



polarizations of the pump and probe pulses, ionization from the ground state to the  $^3B_2$  state (XT channel) or ionization from the electronically excited state to the  $^1A_1$  state (AS channel) is dominant. The latter channel is only active for angles between  $85^\circ$  and  $105^\circ$ , as in this region the  $^1A_1$  state is dominated by the  $(\dots)(b_2)^0(a_1)^2$  configuration.

The time-dependent population of the diabatic  $\tilde{A}^2B_2$  state is shown on the lower right-hand side of Fig. 7. After 11 fs the wave packet in the  $\tilde{A}^2B_2$  state has crossed the conical intersection diabatically, i.e. it remained on the same diabatic surface retaining its electronic character. When the wave packet reaches the inner turning point in the bending coordinate, it has expanded significantly along both bond-stretching coordinates. The asymmetric stretching mode is responsible for vibronic coupling between the  $\tilde{X}$  and  $\tilde{A}$  states. For zero excursion along the asymmetric stretching mode, the molecule belongs to the  $C_{2v}$  point group and the coupling between the  $\tilde{X}$  and  $\tilde{A}$  states vanishes by symmetry. When the molecule has unequal bond lengths, it belongs to the  $C_s$  point group in which the two electronic states have the same  $A'$  symmetry, mix and repel each other. Upon the second return to the conical intersection, the crossing therefore occurs with strong population transfer to the  $\tilde{X}^2A_1$  ground state. Subsequent crossings of the conical intersection are also found to proceed adiabatically, as can be expected from the significant extension along the bond stretch coordinates [56].

Experimental data for the evolution of diffracted and non-diffracted high harmonics (upper panel) for perpendicular (left-hand side) and parallel (right-hand side) polarizations of the pump and probe pulses are shown in Fig. 8. For the case of cross-polarized pump and probe pulses counter-phased modulations of the diffracted ( $m=1$ ) and non-diffracted ( $m=0$ ) harmonic intensities are observed over the first 200–300 fs, followed by smooth variations. The most characteristic features of the diffracted signal is a global intensity maximum around 30–40 fs, a minimum around 70 fs and another maximum around 130 fs. In the case of parallel polarization of the pump and probe pulses, the region of temporal overlap is dominated by wave mixing of the 800 nm and 400 nm beams causing a high intensity of the harmonic signal in  $m=1$ . For longer delays, modulations are hardly visible. The upper panel of Fig. 9 shows a close up on the experimental results in H13, H15 and H18. As even harmonics are only visible for a temporal overlap of the 800 nm and 400 nm fields, their appearance allows an accurate determination of the zero time delay and the cross correlation function as discussed in Section 3.3.

We now analyze these findings by comparing them to simulations. Non-diffracted and diffracted harmonic intensities are calcu-

lated according to Eqs. (12) and (13) using Eq. (5). The necessary quantities entering Eq. (5) are obtained as follows. The ionization rates are calculated by solving the TDSE in the Hartree potential of the channel-dependent cation state [30,19]. The recombination dipoles are obtained from quantum scattering calculations in the Hartree potentials using the eikonal approximation. The nuclear wave packets are assumed to be Gaussian functions of the bond-angle coordinate with  $30^\circ$  FWHM, and the motion of their center is as shown in Fig. 7. The diabatic populations are obtained from wave packet calculations reported in Ref. [56]. As in the case of  $Br_2$ , the propagation phase entering the complex dipole must be computed by averaging the exponential propagation phase term (and not the ionization potential) over the wave packet, thus taking into account the significant extension of the wave packet along all three coordinates of the system. We recall that in  $Br_2$ , the wave-packet spreading caused a significant reduction of the observed modulation depth and a self-interference that reduced the emission amplitude from the excited state for early times.

In a first step, we neglect the temporal variation of the high-harmonic phases and amplitudes and use their average over a Gaussian nuclear wave function in  $\beta$  localized at the minimum of the diabatic state surfaces. Thus, only the time dependence of the populations is retained. These calculations are shown in the lower panel of Fig. 9. The calculations reproduce the main observations of counter-phased oscillations in the diffracted and non-diffracted signals in the case of crossed polarizations and the absence of such modulations in the case of parallel polarizations. However, the calculated oscillations are faster than those observed in the experiment. This could either be due to insufficient accuracy of the potential energy surfaces or to the over-simplification of our theoretical model. On this simple level of interpretation, the observed dynamics thus mostly reflect the diabatic population dynamics, i.e. the evolution of the electronic character of the excited molecule with time. We note that this situation is thus markedly different from  $Br_2$ , where the excited state population is constant over time and the observed modulations are caused by temporal variations of amplitudes and phases of the excited state emission.

In a second step, we now improve the model outlined above by including the temporal variation of the propagation phase term into Eqs. (12) and (13), but still neglecting the temporal variation of the ionization rates and recombination matrix elements. We compare the population of the excited  $\tilde{A}^2B_2$  state (upper panel in Fig. 10) with the simulated (non-diffracted and diffracted) harmonic signal (central panel) and the propagation term  $\langle e^{-i\Delta E_{\tilde{A}^2B_2}^{(R)}\tau} \rangle$  (with  $\tau = 1$  fs) for the AT channel (lower panel). In this case the

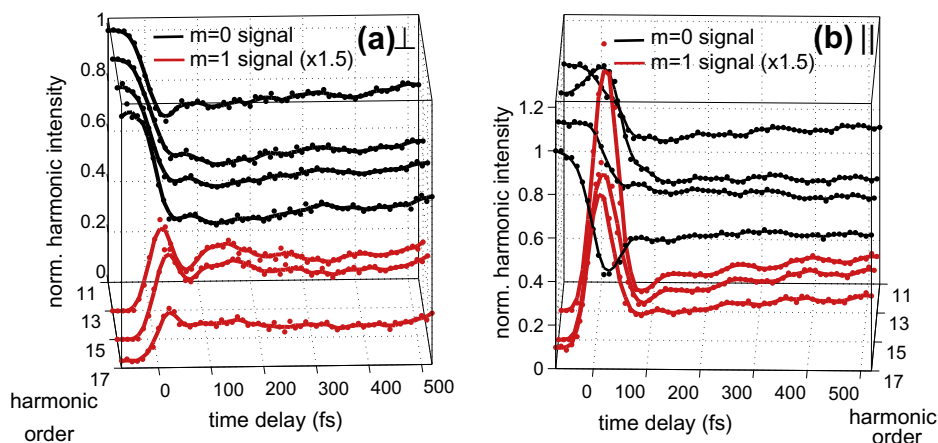
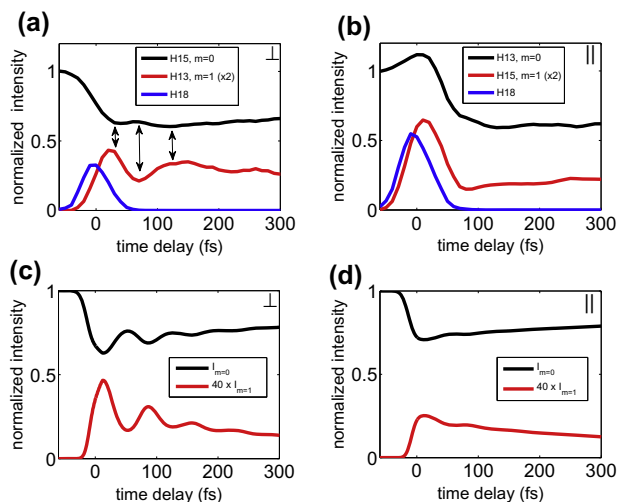


Fig. 8. Experimental data of the diffracted and non-diffracted signals of high-harmonic generation in a transient grating of excited  $NO_2$  molecules as a function of the pump-probe delay. The panels correspond to (a) perpendicular and (b) parallel polarization of pump- and probe pulses. The data was taken from Ref. [56].



**Fig. 9.** Experimental (upper panel) and theoretical data (lower panel) of the diffracted and non-diffracted signals of high-harmonic generation in a transient grating of excited  $\text{NO}_2$  molecules as a function of the pump–probe delay. The panels correspond to (a) perpendicular and (b) parallel polarizations of pump and probe pulses. The theoretical data were calculated by neglecting the time-dependence of phases and amplitudes, only retaining the time-dependent populations. The experimental data is from Ref. [56].

propagation term was averaged over the full three-dimensional coordinate space using the nuclear wave packets associated with diabatic electronic states obtained from calculations [54,56] (see Fig. 11).

The phase  $\Delta I_p^{AT} \tau$  varies almost linearly from  $-2$  to  $+3$  radians when the bond angle decreases from  $134^\circ$  to  $85^\circ$ . The coordinate-averaged phase term has an initial phase angle of  $-1.5$  rad which then rapidly approaches zero, tracing the spreading of the wave packet. The amplitude of the phase term is initially around 0.4 and also rapidly decreases. Both the amplitude and the phase show non-periodic variations following their initial decrease.

The intensities in  $m = 0$  and  $m = 1$  predicted by this improved model still modulate in phase opposition and their comparison with the A-state population dynamics shows that the latter still play an important role in defining the occurrence of maxima and minima. However, the modulation depth is greatly reduced compared to the results shown in the lower panel of Fig. 9. The extrema of the signal described above are captured by the calculation, i.e. a maximum around 10 fs and changes in the slope of the signal around 55 fs and 85 fs in agreement with a population minimum and maximum. However, an amplitude maximum of the propagation term due to constructive interference at 110 fs is also still visible in our model of the non-diffracted harmonic signal. The agreement of the experimental data with the simpler model outlined above is more satisfactory, but the present models need further improvements.

For longer time delays, all population from the excited  $\tilde{A}^2B_2$  state has returned into the  $\tilde{X}^2A_1$  state. Those molecules that have absorbed a photon with energy above the dissociation threshold (3.1155 eV, 397.95 nm vacuum wavelength) can dissociate on the ground state surface. This dissociation takes place on the picosecond time scale and follows simple first-order kinetics [57,58]. On the time scale, where the unimolecular dissociation takes place, the wave packet dynamics of the molecule is so complicated due to its very large extension in coordinate space that the coordinate-dependent quantities entering Eq. (5) can be safely approximated with their time-independent average over all of occupied coordinate space. Consequently, the kinetics of the  $\text{NO}_2$  decomposition are modeled using Eqs. (12) and (13) with the  $\tilde{d}_i(\Omega, t)$  chosen

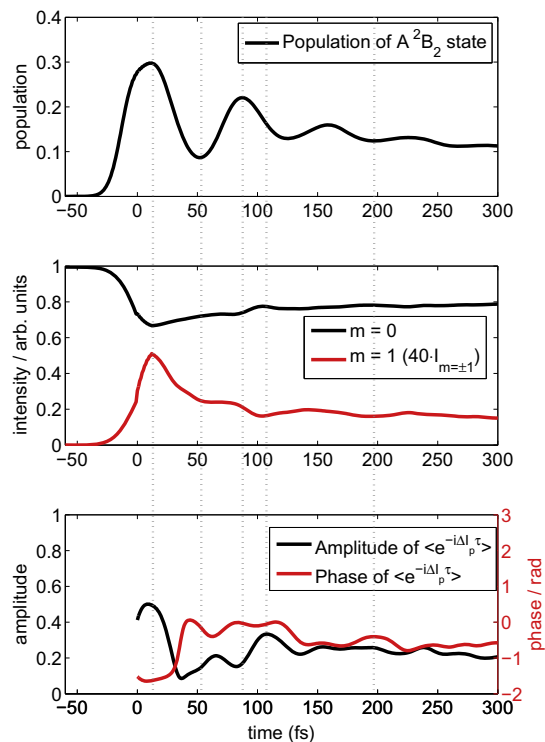


**Fig. 10.** Comparison of the population of the diabatic  $\tilde{A}^2B_2$  in  $\text{NO}_2$  (upper panel) with the calculated high-harmonic signal as function of pump–probe delay for perpendicular polarizations of pump and probe pulses (central panel) and the amplitude and phase of the propagation term for the AT channel. The propagation term was obtained by averaging over the three-dimensional nuclear wave packet. The evolution of the harmonic signal was calculated by using these propagation terms for both the AT and the XS channels.

to be time-independent, and the two possible states  $i$  being the vibrationally excited molecules in the  $\tilde{X}^2A_1$  state and the pair of fragments  $\text{NO}(\tilde{X}^2\Pi) + \text{O}(\tilde{X}^3P)$ , respectively. For molecules excited below the dissociation threshold, the radiated XUV field can be described by

$$E_{\text{XUV}}(\Omega, t) = (1 - r(t))d_g e^{i\phi_g} + r(t)d_e e^{i\phi_e}, \quad (14)$$

where  $t$  is the time elapsed since excitation,  $r(t)$  is the spatially modulated fraction of excited molecules with a smoothed-step temporal evolution,  $d_g$ ,  $d_e$  and  $\phi_g$ ,  $\phi_e$  are the high-harmonic amplitudes and phases of the unexcited and vibrationally excited molecules in the  $\tilde{X}^2A_1$  state, respectively. Those molecules that were excited above threshold can undergo dissociation into  $\text{NO}(\tilde{X}^2\Pi) + \text{O}(\tilde{X}^3P)$  that, together, emit harmonics with a resultant amplitude  $d_f$  and phase  $\phi_f$ . The radiated XUV field is then given by

$$E_{\text{XUV}}(\Omega, t) = (1 - r(t))d_g e^{i\phi_g} + r(t) * e^{-t/t_d} d_e e^{i\phi_e} + r(t) * (1 - e^{-t/t_d}) d_f e^{i\phi_f}, \quad (15)$$

where  $t_d$  is the time constant of the unimolecular dissociation and  $*$  denotes the convolution operation. The analysis and results have been given in Ref. [19], Table 1 of which is reproduced here.

We will now interpret the results summarized in Table 1. We find that the strong-field ionization rate of the excited molecules exceeds that of unexcited ground state molecules by a factor of 4.5. This might be surprising at first sight since strong-field ionization must be governed by vertical ionization potentials which would be identical for vibrationally excited and unexcited molecules if the neutral and cation surfaces were parallel. However, the surfaces are of course not parallel, which means that the Franck–Condon factors for unexcited and vibrationally excited

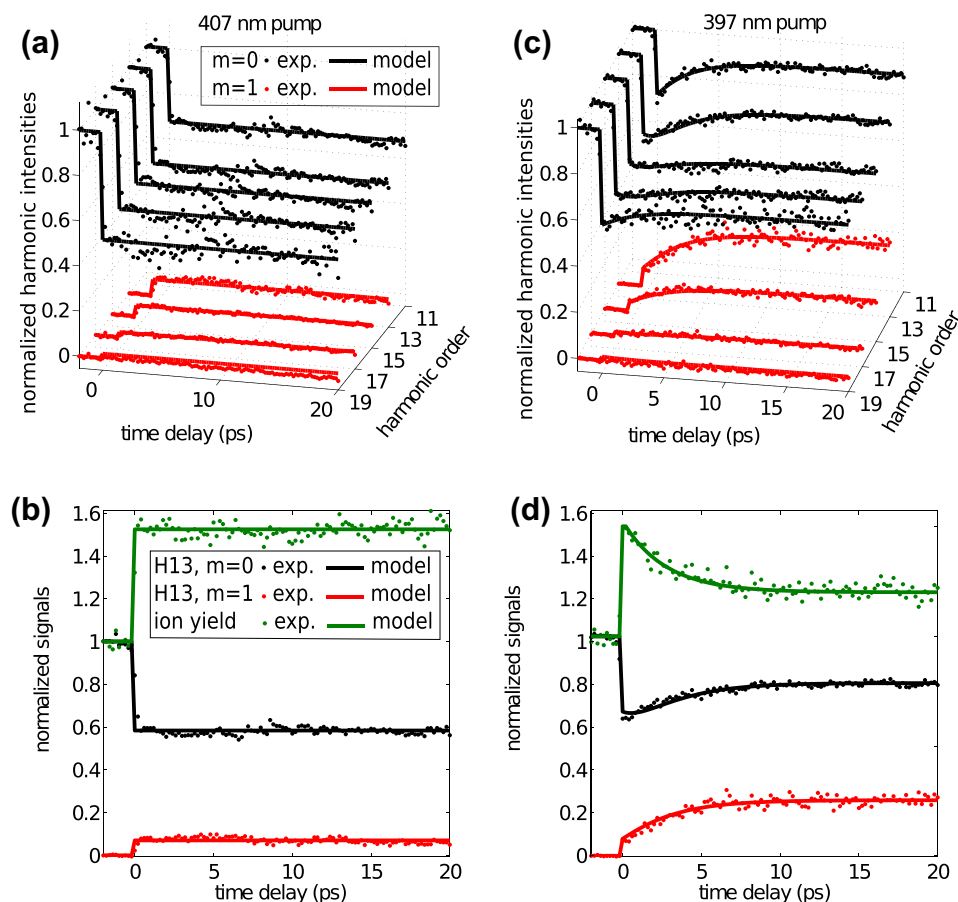


**Fig. 11.** High-harmonic and ion yields as a function of the delay between two synchronized near-UV pump pulses setting up a transient grating of excited  $\text{NO}_2$  molecules and an 800-nm probe pulse generating high harmonics in the excited sample. The yield of diffracted (red dots) and non-diffracted (black dots) high-harmonic signals, normalized to the non-diffracted signal at negative pump-probe delays, for excitation by 407-nm pump pulses is shown in panel (a). The full lines represent the results of the theoretical model described in Eqs. (14) and (15). H13,  $m = 0$ , and  $m = 1$  from (a) together with the total ion yield measured in parallel to the experiment (green dots) and the theoretical model (green line) is shown in panel (b). Panels (c) and (d) show the same observables as panels (a) and (b), but for a pump pulse centered at 397.2 nm. The polarizations of pump and probe are parallel. The data is taken from Ref. [19]. (For interpretation of the references to colour in this figure legend, the reader is referred to the web version of this article.)

molecules will be different. In  $\text{NO}_2$ , vibrational excitation in the range of 3.1 eV allows the excited molecules to reach molecular configurations around linearity, where the ionization potential approaches 9 eV (see Fig. 7), significantly lower than the vertical ionization potential from the ground electronic state of 11.2 eV. These configurations will dominate the observed ionization rate. Using ADK ionization rates, we find that in a laser field of intensity  $1 \times 10^{14} \text{ W/cm}^2$ , the observed increase of the ionization rate by a factor of 4.5 would correspond to an ionization potential of 7.5 eV, which is significantly lower than expected. We note that this consideration neglects the influences of configuration mixing and the orbital shape on the ionization rates. The ionization rate of the  $\text{NO} + \text{O}$  pair will be dominated by  $\text{NO}$ , given the ionization

potentials of 9.2 and 13.8 eV, respectively. The 2.3 times higher ionization rate of  $\text{NO} + \text{O}$  compared to unexcited  $\text{NO}_2$  is exactly consistent with the ratio of ADK rates of  $\text{NO}$  vs.  $\text{NO}_2$ . Looking at the variation of the amplitudes with high-harmonic orders, the decrease of the relative amplitudes of the  $\text{NO} + \text{O}$  pair is particularly striking. This is consistent with the lower cut-off energy of the high harmonics that will be emitted from a low- $I_p$  target such as  $\text{NO}$  because of ionization saturation.

Since the ionization rates and high-harmonic amplitudes have both been measured, we can determine an ionization-corrected high-harmonic amplitude  $d' = (d/d_g)/\sqrt{i/i_g}$  which would then mostly reflect the relative amplitudes of the photorecombination matrix elements. For  $\text{NO}_2$  excited at 397 nm,  $d'$  has the values

**Table 1**  
High-harmonic amplitudes and phases and strong-field ionization rates of vibrationally excited  $\text{NO}_2$  molecules in the  $\tilde{X}^2A_1$  state or  $\text{NO}(^2II) + \text{O}(^3P)$  fragment pairs obtained in the photodissociation of  $\text{NO}_2$ . The center wavelength of the photodissociation laser pulse is indicated in parentheses.

Species	$i/i_g$	H13		H15		H17	
		$d/d_g$	$ \phi - \phi_g (\text{rad})$	$d/d_g$	$ \phi - \phi_g (\text{rad})$	$d/d_g$	$ \phi - \phi_g (\text{rad})$
$\text{NO}_2^+$ (407 nm)	4.5	3.0	2.03	2.3	2.02	1.2	2.24
$\text{NO}_2^+$ (397 nm)	4.5	3.2	1.94	2.1	1.92	1.1	4.22
$\text{NO} + \text{O}$ (397 nm)	2.3	6.1	2.09	4.1	2.00	1.4	1.87
$t_d = 2.71 \pm 0.15 \text{ ps}$							

1.5, 1.0 and 0.5 for H13, H15 and H17, respectively. This shows that the photorecombination matrix elements are not much different between the vibrationally excited NO<sub>2</sub> molecules and the ground state molecules. The rapid decrease of  $d'$  with harmonic order is consistent with a lower effective  $I_p$  for the vibrationally excited molecules, resulting in a lower cut-off energy. For the NO + O pair,  $d'$  takes the values 4.0, 2.7 and 0.9. In this case, the photorecombination matrix element for low harmonics is larger than that of unexcited NO<sub>2</sub> which might originate in the fact that the relevant NO orbital has a simpler spatial structure than that of NO<sub>2</sub>, resulting in a larger absolute value of the photo recombination matrix element.

Finally, we also discuss the relative high-harmonic phases which result from the combination of the propagation phase  $I_p\tau$  and the phase of the photorecombination matrix elements. Using  $\tau \approx 1$  fs, which is adequate for H13 for an intensity of  $1 \times 10^{14}$  W/cm<sup>2</sup> and an  $I_p$  of 11.2 eV, we find that the effective  $I_p$  of NO<sub>2</sub> excited at 397 nm is 10.0 eV or 5.91 eV ( $2\pi$  ambiguity in the phase) under the assumption that the phases of the photorecombination matrix elements are unchanged in the vibrationally excited state. Turning the procedure around, we would expect that H13 emitted by NO has a propagation phase shift of  $|\Delta I_p\tau| \approx 3.1$  rad. The difference between this number and the measured 2.09 rad can most likely be attributed to a recombination phase difference between NO and unexcited NO<sub>2</sub>.

## 6. Conclusions

The present review of experimental data from TRHHS and their comparison with general model calculations has illustrated the principles and mechanisms of the method. The method is related to time-resolved photoelectron spectroscopy through the nature of the photorecombination matrix elements. The main novelty of TRHHS is its coherent nature which makes it highly sensitive to small excited state populations and to the phase of photorecombination matrix elements. We have shown that TRHHS is sensitive to the variation of the vertical ionization potential along the reaction coordinate, which will be useful for probing chemical dynamics that is predominantly taking place along a single soft coordinate. In larger molecules with dynamics taking place in a coordinate space of higher dimensionality, the distribution of vertical ionization energies will often be sufficiently broad that the variation of the latter with pump-probe delay becomes less significant. In this case, the method enables the observation of the population dynamics in diabatic states, i.e. the temporal evolution of the electronic character of the excited molecule undergoing dynamics. We expect that the latter property will transfer to other polyatomic molecules and will be a useful property in studying non-adiabatic dynamics in other systems. The present method might in the future be extended to probing the electronic structure of unsaturated hydrocarbon molecules undergoing pericyclic reactions. Moreover, time-resolved high-harmonic spectroscopy may also be used as technique unifying pump (ionization) and probe (recombination) in a single laser cycle to observe attosecond dynamics in electronically excited systems.

## Acknowledgements

We thank J. Bertrand, D. Villeneuve and P. Corkum (NRC, Ottawa) and B. Fabre, J. Higuette, H. Ruf, A. Dubrouil and E. Constant (CE-LIA, Bordeaux) for discussions and their contributions to the experimental work described here. We thank Y. Arasaki and K. Takatsuka (Tokyo University) for performing the wave packet calculations on NO<sub>2</sub> and S. Patchkovskii and M. Spanner (NRC, Otta-

wa) for the calculations of strong-field ionization rates and photorecombination dipoles of NO<sub>2</sub>.

This work was supported by the Swiss National Science Foundation (SNSF) under project PPOOP2\_128274 and by ETH Research Grant ETH-33 10-3.

## References

- [1] J. Manz, L. Wöste (Eds.), *Femtochemistry*, VCH Verlagsgesellschaft, Weinheim, 1995.
- [2] A.H. Zewail, *J. Phys. Chem. A* 104 (24) (2000) 5660.
- [3] R. Neutze, R. Wouts, D. van der Spoel, E. Weckert, J. Hajdu, *Nature* 406 (6797) (2000) 752.
- [4] H.N. Chapman, P. Fromme, A. Barty, T.A. White, R.A. Kirian, A. Aquila, M.S. Hunter, J. Schulz, D.P. DePonte, U. Weierstall, et al., *Nature* 470 (7332) (2011) 73.
- [5] H. Ihee, V.A. Lobastov, U.M. Gomez, B.M. Goodson, R. Srinivasan, C.-Y. Ruan, A.H. Zewail, *Science* 291 (5503) (2001) 458.
- [6] B.J. Siwick, J.R. Dwyer, R.E. Jordan, R.J.D. Miller, *Science* 302 (5649) (2003) 1382.
- [7] A. Stolow, A.E. Bragg, D.M. Neumark, *Chem. Rev.* 104 (4) (2004) 1719.
- [8] C. Bressler, M. Chergui, *Ann. Rev. Phys. Chem.* 61 (1) (2010) 263.
- [9] J.A. Davies, R.E. Continetti, D.W. Chandler, C.C. Hayden, *Phys. Rev. Lett.* 84 (2000) 5983.
- [10] T. Seideman, *Ann. Rev. Phys. Chem.* 53 (1) (2002) 41.
- [11] A. Stolow, *Int. Rev. Phys. Chem.* 22 (2003) 377.
- [12] O. Gessner, A. Lee, J. Shaffer, H. Reisler, S. Levchenko, A. Krylov, J.G. Underwood, H. Shi, A. East, D. Wardlaw, et al., *Science* 311 (2006) 219.
- [13] C.Z. Bisgaard, O.J. Clarkin, G. Wu, A.M.D. Lee, O. Gessner, C.C. Hayden, A. Stolow, *Science* 323 (5920) (2009) 1464.
- [14] N.L. Wagner, A. Wüest, I.P. Christov, T. Popmintchev, X. Zhou, M.M. Murnane, H.C. Kapteyn, *Proc. Natl. Acad. Sci.* 103 (36) (2006) 13279.
- [15] W. Li, X. Zhou, R. Lock, S. Patchkovskii, A. Stolow, H.C. Kapteyn, M.M. Murnane, *Science* 322 (5905) (2008) 1207.
- [16] Z.B. Walters, S. Tonzani, C.H. Greene, *Chem. Phys.* 366 (1–3) (2009) 103.
- [17] H.J. Wörner, J.B. Bertrand, P.B. Corkum, D.M. Villeneuve, *Phys. Rev. Lett.* 105 (10) (2010) 103002.
- [18] H.J. Wörner, J.B. Bertrand, D.V. Kartashov, P.B. Corkum, D.M. Villeneuve, *Nature* 466 (7306) (2010) 604.
- [19] H.J. Wörner, J.B. Bertrand, B. Fabre, J. Higuette, H. Ruf, A. Dubrouil, S. Patchkovskii, M. Spanner, Y. Mairesse, V. Blanchet, et al., *Science* 334 (6053) (2011) 208.
- [20] H.J. Wörner, H. Niikura, J.B. Bertrand, P.B. Corkum, D.M. Villeneuve, *Phys. Rev. Lett.* 102 (10) (2009) 103901.
- [21] T. Morishita, A.-T. Le, Z. Chen, C.D. Lin, *Phys. Rev. Lett.* 100 (1) (2008) 013903.
- [22] A.-T. Le, R.R. Lucchese, S. Tonzani, T. Morishita, C.D. Lin, *Phys. Rev. A* 80 (1) (2009) 013401.
- [23] O. Smirnova, Y. Mairesse, S. Patchkovskii, N. Dudovich, D.M. Villeneuve, P.B. Corkum, M.Y. Ivanov, *Nature* 460 (7258) (2009) 972.
- [24] P. Eckle, A.N. Pfeiffer, C. Cirelli, A. Staudte, R. Dörner, H.G. Muller, M. Büttiker, U. Keller, *Science* 322 (5907) (2008) 1525.
- [25] M. Lewenstein, P. Balcou, M.Y. Ivanov, A. L'Huillier, P. Corkum, *Phys. Rev. A* 49 (1994) 2117.
- [26] T. Kanai, E.J. Takahashi, Y. Nabekawa, K. Midorikawa, *Phys. Rev. Lett.* 98 (2007) 153904.
- [27] J.B. Bertrand, H.J. Wörner, H.-C. Bandulet, E. Bisson, M. Spanner, J.-C. Kieffer, D.M. Villeneuve, P.B. Corkum, *Phys. Rev. Lett.* 106 (2011) 023001.
- [28] J. Muth-Böhm, A. Becker, F.H.M. Faisal, *Phys. Rev. Lett.* 85 (11) (2000) 2280.
- [29] X.M. Tong, Z.X. Zhao, C.D. Lin, *Phys. Rev. A* 66 (2002) 033402.
- [30] M. Spanner, S. Patchkovskii, *Phys. Rev. A* 80 (2009) 063411.
- [31] A.-T. Le, R.R. Lucchese, M.T. Lee, C.D. Lin, *Phys. Rev. Lett.* 102 (20) (2009) 203001.
- [32] R.R. Lucchese, G. Raseev, V. McKoy, *Phys. Rev. A* 25 (1982) 2572.
- [33] A.F. Starace, *Handbuch der Physik*, vol. 31, Springer, Berlin, 1981 (Ch. Theory of atomic photoionization).
- [34] S. Minemoto, T. Umegaki, Y. Oguchi, T. Morishita, A.-T. Le, S. Watanabe, H. Sakai, *Phys. Rev. A* 78 (6) (2008) 061402(R).
- [35] A.D. Shiner, B. Schmidt, C. Trallero-Herrero, Wörner, S. Patchkovskii, P.B. Corkum, J.-C. Kieffer, F. Légaré, D.M. Villeneuve, *Nat. Phys.* 7 (2011) 464.
- [36] H.J. Wörner, J.B. Bertrand, P. Hockett, P.B. Corkum, D.M. Villeneuve, *Phys. Rev. Lett.* 104 (23) (2010) 233901.
- [37] M.V. Frolov, N.L. Manakov, T.S. Sarantseva, M.Y. Emelin, M.Y. Ryabikin, A.F. Starace, *Phys. Rev. Lett.* 102 (24) (2009) 243901.
- [38] Ch. Jungen (Ed.), *Molecular Applications of Quantum Defect Theory*, Institute of Physics Publishing, Bristol, Philadelphia, 1996.
- [39] S. Sukiasyan, S. Patchkovskii, O. Smirnova, T. Brabec, M.Y. Ivanov, *Phys. Rev. A* 82 (2010) 043414.
- [40] G.L. Yudin, A.D. Bandrauk, P.B. Corkum, *Phys. Rev. Lett.* 96 (6) (2006) 063002.
- [41] S. Baker, J.S. Robinson, C.A. Haworth, H. Teng, R.A. Smith, C.C. Chirila, M. Lein, J.W.G. Tisch, J.P. Marangos, *Science* 312 (2006) 424.
- [42] Y. Mairesse, D. Zeidler, N. Dudovich, M. Spanner, J. Levesque, D.M. Villeneuve, P.B. Corkum, *Phys. Rev. Lett.* 100 (14) (2008) 143903.
- [43] D.J. Tannor, *Introduction to Quantum Mechanics: A Time-Dependent Perspective*, University Science Books, Sausalito, 2007.

- [44] T.P. Rakitzis, T.N. Kitsopoulos, *J. Chem. Phys.* 116 (21) (2002) 9228.
- [45] R.J. Le Roy, R.G. Macdonald, G. Burns, *J. Chem. Phys.* 65 (4) (1976) 1485.
- [46] H.D. Cohen, U. Fano, *Phys. Rev.* 150 (1966) 30.
- [47] D. Rolles, M. Braune, S. Cvejanovic, O. Geszner, R. Hentges, S. Korica, B. Langer, T. Lischke, G. Prumper, A. Reinkoster, et al., *Nature* 437 (7059) (2005) 711.
- [48] M. Lein, N. Hay, R. Velotta, J. Marangos, P. Knight, *Phys. Rev. Lett.* 88 (2002) 183903.
- [49] C. Vozzi, M. Negro, F. Calegari, G. Sansone, M. Nisoli, S. De Silvestri, S. Stagira, *Nature Physics Advance Online Publication*, 2011, DOI:10.1038/NPHYS2029.
- [50] H.J. Wörner, *Chimia* 65 (5) (2011) 299.
- [51] W. Li, A.A. Jaron-Becker, C.W. Hogle, V. Sharma, X. Zhou, A. Becker, H.C. Kapteyn, M.M. Murnane, *Proc. Natl. Acad. Sci.* 107 (47) (2010) 20219.
- [52] F. Santoro, C. Petrongolo, *J. Chem. Phys.* 110 (9) (1999) 4419.
- [53] S. Mahapatra, H. Köppel, L.S. Cederbaum, P. Stampfuhl, W. Wenzel, *Chem. Phys.* 259 (2-3) (2000) 211.
- [54] Y. Arasaki, K. Takatsuka, *Chem. Phys.* 338 (2-3) (2007) 175.
- [55] Y. Arasaki, K. Takatsuka, K. Wang, V. McKoy, *J. Chem. Phys.* 132 (12) (2010) 124307.
- [56] P.M. Kraus, Y. Arasaki, J.B. Bertrand, P.B. Corkum, D.M. Villeneuve, K. Takatsuka, H.J. Wörner, *Phys. Rev. A* (submitted for publication).
- [57] S.I. Ionov, G.A. Brucker, C. Jaques, Y. Chen, C. Wittig, *J. Chem. Phys.* 99 (5) (1993) 3420.
- [58] B. Abel, B. Kirmse, J. Troe, D. Schwarzer, *J. Chem. Phys.* 115 (2001) 6522.